Hydrodynamic Slip Characteristics of Shear-Driven Water Flow in Nanoscale Carbon Slits

Abdul Aziz Shuvo, Luis E. Paniagua-Guerra, Xiang Yang, and Bladimir Ramos-Alvarado*
Department of Mechanical Engineering, The Pennsylvania State University, University Park, Pennsylvania, 16802, USA.
*Corresponding author: bzr52@psu.edu

Abstract

This work reports on the effects of shear rate and interface modeling parameters on the hydrodynamic slip length (L_S) for water-graphite interfaces calculated using non-equilibrium molecular dynamics. Five distinct non-bonded solid-liquid interaction parameters were considered to assess their impact on L_S. The interfacial force field derivations included sophisticated electronic-structure-calculation-informed and empirically determined parameters. All interface models exhibited a similar and bimodal L_S response when varying the applied shear rate. L_S in the low shear rate regime (LSR) is in good agreement with previous calculations obtained through equilibrium molecular dynamics. As the shear rate increases, L_S sharply increases and asymptotes to a constant value in the high shear regime (HSR). It is noteworthy that L_S in both, the LSR and HSR can be characterized by the density depletion length, whereas solid-liquid adhesion metrics failed to do so. For all interface models, L_{HSR} calculations were, on average, ~28% greater than L_{LSR}, and this slip jump was confirmed using the SPC/E and TIP4P/2005 water models. To address the L_S transition from the LSR to HSR, the viscosity of water and the interfacial friction coefficient were investigated. It was observed that in the LSR, viscosity and the friction coefficient decreased at a similar rate, while in the LSR-to-HSR transition the friction coefficient decreased at a faster rate than the shear viscosity until they reached a new equilibrium; hence, explaining the L_S-bimodal behavior. This study provides valuable insights into the interplay between interface modeling parameters, shear rate, and rheological properties in understanding hydrodynamic slip behavior.

1. Introduction

The convergence of nanotechnology and fluid dynamics has emerged as a new scientific discipline known as nanofluidics, which has aided in the development of ultrafiltration,[1,2] water desalination,[3–5] enhancement of ion transport,[6–9] and various biological applications.[10,11] Consequently, fluid flow at the nanoscale has prompted significant interest among researchers owing to its remarkable range of applications. Fluid flow in nanoscale conduits exhibits distinct characteristics compared to its behavior at the macroscale. This discrepancy arises from the higher surface-to-volume ratio and the resulting influence of interfaces.

Unquestionably, the no-slip boundary condition combined with the Navier-Stokes equations represents a cornerstone of classical fluid dynamics. And while the Navier-Stokes equation can describe flows at scales as small as ~ 1 nm,[12,13] the underlying basis for the no-slip boundary condition is still empirical and without a foundation in physical principles.[14] It is worth noting that nanoscale flows exhibit slip[15] and can be characterized by a first-order slip boundary condition[16]

$$u_s = L_S \left.\frac{\partial u}{\partial \zeta}\right|_{\zeta} \tag{1}$$

where u_s and L_S are the slip velocity and slip length, respectively, and ζ indicates the coordinate normal to the solid-liquid interface. L_S is the distance over which the linear extrapolation of the velocity yields a no-slip condition; thus, $L_S = 0$ indicates the traditional no-slip condition.

Based on the principles of fluid dynamics, an inverse relationship exists between flow resistance and the size of the flow channel. Therefore, nanofluidic systems are expected to require more pumping power to facilitate fluid flow. Nonetheless, hydrodynamic slip in nanochannels has been reported,[17,18] causing deviations from theoretical expectations. Recently, hydrodynamic slip has been the focus of studies aiming to reduce friction in nanofluidic systems[19] and friction reduction in some applications of bearings and rotating shafts.[20,21] As such, a thorough understanding of slip behavior is necessary; particularly, the concept of slip at high shear rates is yet to be fully understood.

Early non-equilibrium molecular dynamics (NEMD) investigations demonstrated a notable lack of consistency regarding the effect of shear rate on L_S. Several investigations reported unbounded slip growth at high shear rates[22–26], whereas others have shown a reduction in L_S at high shear rates[27,28]. Martini et al.[29] performed a set of simulations to analyze and compare the behavior of L_S at high shear rates. When only the liquid atoms were thermostated, and the solid walls were frozen (rigid wall model), they observed that L_S exponentially grew with shear rate. Conversely, the growth of L_S was bounded at high shear rates in a flexible wall model where solid atoms were allowed to vibrate to dissipate viscous heating, which is consistent with the experimental measurements of L_S reported by Li et al.[30].

Previous contributions[23,24,28] reported that L_S calculations using NEMD in the low shear rate limit could be accurately matched by equilibrium molecular dynamics (EMD)[23,24,28]. The NEMD method computes L_S from the velocity profile of a fluid by applying a shear rate or pressure gradient to the fluid, where larger than experimental shear rates and pressure gradients must be applied to bypass the timescale limitations of MD models and damp statistical noise. Therefore, the NEMD method strongly relies on a proper thermostating approach[29,31], i.e., a computational artifact to control the flow-driving-force-induced temperature rise without affecting the physics of the system. Recently, Oga et al.[32] introduced a fitted Green-Kubo integral designed for the timescale range exhibiting slow decay over time to estimate the friction coefficient in NEMD. This EMD approach could compute the friction coefficient of NEMD at a shear rate of approximately ~10^9 s^{-1}, representing the low shear rate limit.

Similarly, NEMD simulations using the transient-time correlation function (TTCF) technique have been introduced to probe realistic low shear rates effectively but at a large computational cost.[33,34]

The numerical calculations of L_S are significantly influenced by the solid-liquid interaction force field (interface affinity). Voronov et al.[22,35] artificially altered the surface wettability of MD models by adjusting the Lennard-Jones (LJ) solid-liquid interaction parameters (ϵ_r and σ_r). They found that hydrophobic surfaces generated by lowering ϵ_r (interaction energy strength) with fixed σ_r (fixed equilibrium fluid distance) resulted in large L_S, whereas hydrophobic surfaces generated by increasing σ_r while keeping ϵ_r led to small changes in slip. More notably, Huang et al.[36] proposed a quasi-universal scaling relation, where L_S for different wettability appeared to follow $L_S \sim (1+\cos\theta)^{-2}$, where θ is the surface's contact angle. Conversely, Ho et al.[37] artificially modified the wettability of MgO by changing its lattice constant and found that L_S increased for more hydrophilic surfaces, thus challenging the validity of the quasi-universal relation. To alleviate these slip-wettability inconsistencies, the density depletion length δ, an interfacial liquid structure metric that accounts for the availability of momentum carriers, has been used to describe the trends in L_S[38–40]. The density depletion length (δ) can be calculated using Eq. (2)[40]:

$$\delta = \int_0^\infty \left[1 - \frac{\rho_S(z)}{\rho_S^b} - \frac{\rho_L(z)}{\rho_L^b}\right] dz \tag{2}$$

where ρ_S, ρ_L are the solid and liquid densities, and the superscript b indicates a bulk value (far away from the interface). The $z \to \infty$ limit is defined at the point where the bulk liquid density is reached and the value of δ reaches a constant value, and the term $\frac{\rho_S(z)}{\rho_S^b}$ is ignored when $z = 0$ is defined at the innermost solid layer in contact with a liquid. δ serves as a metric that can describe the availability (surplus/deficit) of the momentum carrier liquid molecules at the solid-liquid interface. A high δ indicates a low availability of momentum carriers (molecules) due to low concentration and a large equilibrium distance of water with respect to the solid atoms. Conversely, a lower δ represents greater availability of the carriers near the interface.[39,41]

In this contribution, we conducted NEMD simulations to investigate the characteristics of L_S in Couette flow with shear rates ranging from 1.6×10^{10} to 1.8×10^{11} s^{-1}. To thoroughly study the behavior of L_S, we investigated five distinct graphite-water interface models, where the interaction parameters were determined from (i) matching adsorption energy curves obtained from electronic structure calculations and (ii) empirical matching of wettability conditions. The observed trends in L_S exhibited consistency with both prior NEMD calculations[29] and experimental measurements for a wide range of shear rates[30], thereby validating the reliability of our simulations. In our analysis, we established correlations between δ and L_S in both the low shear rate (LSR) and high shear rate (HSR) regimes. Our calculations for all five interfaces reveal a sharp L_S transition from the LSR to HSR

regime at a narrow range of the applied shear rate, while this transition shifted to higher shear rate values when the fluid shear was considered. Such transition in L_S was attributed to the shift from constant to shear-thinning water viscosity and constant to rapid friction coefficient reduction as the shear rate increased. Furthermore, our study reveals that the LSR-to-HSR L_S jump is seemingly constant for all interface models and two different water models, presenting an unreported aspect of hydrodynamic slip length in nanoconfined shear-driven flow. These results significantly contribute to a more comprehensive understanding of the intricate behavior of L_S in nanoconfined fluid systems.

2. Methodology

2.1 Molecular Dynamics Simulations

We used LAMMPS[42] to model Couette flow of liquid water confined between two solid graphite slabs, and OVITO[43] for visualization; see Figure 1 for an illustration of the model used. The graphite slabs had dimensions of 6.2 nm×5.4 nm in the *x*- and *y*-direction, respectively. Each slab was 2 nm thick and consisted of seven graphene sheets to avoid size effects on the calculation of L_S[44,45]. 5491 water molecules were distributed inside the gap between the solid slabs, $h = 5$ nm, where h was slightly varied to achieve a bulk water density of 1.00 ± 0.02 g/cm^3 in the region away from the interfaces. Subsequently, the system was considered compressibility-free upon attaining the desired density. Figure 2 depicts the water density profiles obtained for the different interface models investigated; see Table 1. The simulation box was periodic in the *x*- and *y*-direction, while the *z*-direction, normal to the flow, was fixed. The outermost graphene sheet in each slab was not integrated (frozen) to maintain the size of the simulation box. Couette flow was implemented by moving the top graphite slab at velocities ranging from 80 m s^{-1} to 900 m s^{-1}, while the bottom slab remained fixed and a Nosè-Hoover[46,47] thermostat was implemented to remove the excess heat using three different approaches. Further discussion about thermostating is presented in Section 2.2.

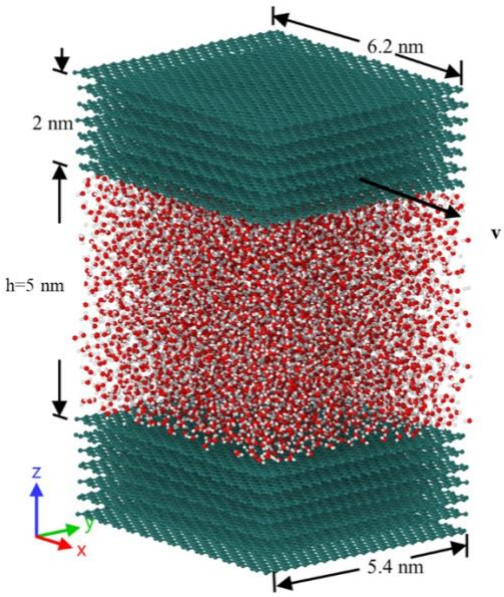

Figure 1. Computational model of the graphite-water nanochannel (red spheres are oxygen atoms, white spheres are hydrogen atoms, and teal spheres are carbon atoms).

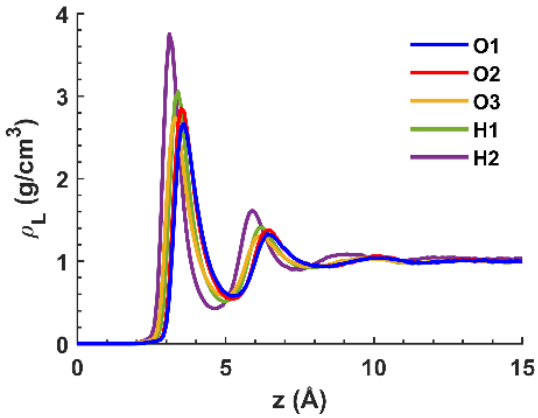

Figure 2. Water density profiles for the different interface models. The innermost graphene sheet is located at z = 0 Å.

The SPC/E water model[48,49] was utilized for the water particles and the SHAKE algorithm was implemented to ensure bond rigidity. The long-range Coulombic interactions were computed using the PPPM[50] algorithm with a precision of 1×10^{-6}. The carbon atoms in each graphene sheet were modeled using a Tershoff[51] force field (FF), while interlayer carbon interactions across different graphene sheets were modeled by a 12-6 LJ FF (ϵ_{CC} = 0.4438 kJ/mol, σ_{CC} = 3.276 Å, and cut-off distance = 15 Å).[52] Similarly, the solid-liquid interactions were modeled using a 12-6 LJ FF with a cut-off distance of 15 Å. Five distinct interface parameter sets were used and are listed in Table 1. The models O1-O3 considered only carbon and oxygen interactions, while H1 and H2 considered both carbon-oxygen and carbon-hydrogen interactions. These LJ parameters were determined using distinct methodologies and optimization techniques. For O3, ϵ_{CO} was systematically adjusted while keeping σ_{CO} constant until achieving a size-independent MD contact angle of θ = 64.4° on a chemically pure graphite surface in atmospheric conditions.[53] Furthermore, the O1 and O2 parameters were derived using the wettability-E_{min} relationship proposed by Ramos-Alvarado.[45] This relationship is an analytical expression derived from theory and verified through MD simulations where the LJ parameters are the inputs, and a size-independent contact angle is the output of the model. Using Ramos-Alvarado's model, we obtained a set of LJ parameters (O1 and O2) that yielded the same contact angle and binding energy (E_{min}) as parameters O3; however, we anticipated different interfacial liquid properties. Hence, it is of great interest to analyze the behavior of Ls in shear-driven flow among interface models O1, O2, and O3. Lastly, the optimization of LJ parameters for H1 was conducted by Ramos Alvarado et al.[45] utilizing a method that required two adsorption energy curves, each for a water monomer in different orientations; thus, eliminating the ambiguity of fitting four parameters using only one adsorption curve. The adsorption energy data for H1 was generated by Ma et al.[54] using random phase approximation

calculations. Lastly, the LJ parameters for H2 were systematically optimized by Wu and Aluru[55] using first principle calculations from CCSD(T)[56]. The LJ parameter optimization for H2 was conducted using a method that relied on a single adsorption energy curve. The contact angles shown in Table 1 were calculated by Paniagua-Guerra et al.[39] The authors utilized cylindrical droplet wettability[53] simulations, where contact line and size effects were addressed.

Table 1. LJ parameters for the different interface models.

Source	ID	ϵ_{CO} (kJ/mol)	σ_{CO}(Å)	ϵ_{CH} (kJ/mol)	σ_{CH}(Å)	δ (Å)[39]	θ (°)[39]	Marker
Paniagua-Guerra et al.[39]	O1	0.3889	3.480	-	-	2.036	64.4	▲
Paniagua-Guerra et al.[39]	O2	0.4046	3.420	-	-	1.967	64.4	●
Ramos-Alvarado et al.[53]	O3	0.4736	3.190	-	-	1.771	64.4	▼
Ramos-Alvarado et al.[45]	H1	0.3268	3.389	0.2033	2.647	1.761	48.4	■
Voloshina et al.[55,56]	H2	0.6887	3.126	0.1029	2.447	1.372	film	★

2.2 Thermostating Strategy

The NEMD method has been used to simulate Couette and Poiseuille flow. However, in atomistic simulations, it is necessary to apply a relatively high shear stress to produce noise-free data due to the short simulation timescale compared to experimental conditions. Consequently, the applied shear in NEMD simulations generates significant heating, requiring a medium to dissipate thermal energy from the system. Previous investigations have identified several thermostating techniques (atomic velocity rescaling algorithms) that effectively remove the excess heat from the system. Some studies have thermostated all solid and liquid atoms,[22,57,58] while in other works, only the fluid atoms are thermostated.[35,59,60] Thermostatting the fluid atoms interrupts the natural flow dynamics by rescaling the fluid particles' velocity, resulting in unphysical flow conditions.[61–63] Contrarily, heat dissipation through the solid wall atoms in a nanochannel is a more physically sound alternative. Past contributions have attempted to mimic the natural process of heat transfer by thermostating only solid atoms in the nanochannel.[23,24,29,64,65] Yong et al.[31] performed molecular dynamics simulations using three distinct thermostat configurations: (i) thermostating only fluid atoms, (ii) thermostating both solid and fluid atoms, and (iii) thermostating only solid atoms. The authors reported a parabolic temperature profile that was consistent with the energy equation by applying the Langevin thermostat in both the top and bottom solid walls. Furthermore, the shear stress and velocity profile remained

constant, as expected from theory. However, the system dynamics deviated from theory when isothermal conditions were imposed on the liquid atoms at high shear rates.[15,31] Thus, thermostating only the solid wall atoms are preferred to facilitate natural cooling, particularly at high shear rates over other thermostating techniques.

In this work, only the bottom solid wall atoms were thermostated at 300 K to model natural cooling, and the top solid wall (adiabatic wall) was exclusively utilized to apply shear in water. Consequently, the observed temperature profiles exhibited a parabolic shape with a null temperature gradient (dT/dz =0) at the top wall, see Figure S1. The solid wall atoms were thermostated in three different ways, as indicated in Figure 3. All graphene sheets of the bottom slab were thermostated in T1, which models direct water cooling in contact with a large isothermal sink. Four graphene and two graphene sheets were thermostated in T2 and T3, respectively, representing cooling with an increasing level of conduction from T2 to T3 to a large isothermal heat sink. The non-thermostated carbon and water atoms were integrated with the microcanonical ensemble (NVE), see Figure 3. The Nosè-Hoover[46,47] thermostat was utilized with a 0.1 ps time constant. Ls was calculated using models T1-T3 and a negligible difference was observed, as reported in Figure S2 of the Supplemental Material. Hence, the T1 thermostating approach was implemented in further calculations.

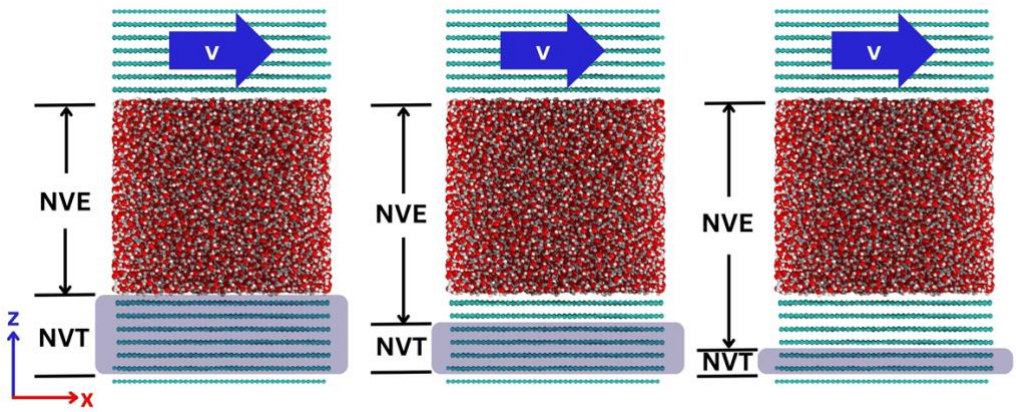

Figure 3. Computational domain schematics indicating the different thermostating approaches.

2.3 Simulation Details

The following steps describe the overall simulation approach: (1) The whole system was equilibrated at 300 K for 1 ns using the canonical ensemble (NVT). (2) To verify stability and equilibration, the whole system was run for another 1 ns in the microcanonical ensemble (NVE), where temperature, pressure, and energy were monitored to ensure steadiness. (3) Following equilibration, shear was applied in the system by moving the top graphite slab at a constant velocity, v, thus creating the applied shear rate defined as $\dot{\gamma}_a = \frac{v}{h}$, where h is the gap between the carbon slabs, and $\dot{\gamma}_a$ ranged from 1.6×10^{10} s^{-1} to 1.8×10^{11} s^{-1}. During the non-equilibrium stage that lasted 2 ns, the carbon atoms in the bottom slab and water atoms were subjected to thermostating as indicated in Figure 3. (4) After

ensuring temperature, pressure, and pressure steadiness in step 3 (see Figure S3 and Figure S4 for simulation stability verification), the system was finally run for 5 ns for data collection. Hereafter, the atomic coordinates, velocities, and forces of the atoms were recorded at intervals of 0.5 ps, and three independent sets of simulations were conducted for the calculations pertinent to this investigation. The time step for all simulations was 1 fs (see Section 4 and Figure S5 of Supplemental Material for more details).

The water confinement was divided into several small bins 5 Å thick in the *z*-direction to calculate the velocity profiles as space and time averages. For further details regarding the domain discretization effect on the calculation of velocity and temperature profiles, please refer to Section 5 and Figure S6 of the Supplementary Material. Figure 4 depicts a schematic of the L_S calculation, where u_s represents the slip velocity right at the solid-fluid interface, $\dot{\gamma}_f = \frac{\partial v}{\partial z}$ is the slope of the velocity profile or the fluid shear rate, and L_S is then calculated as the extrapolation of the slip velocity profile to the location where the no-slip condition would be observed or $L_S = \frac{u_s}{\partial v/\partial z}$. It is noteworthy that the averaged velocity profile was derived from three independent simulation sets.

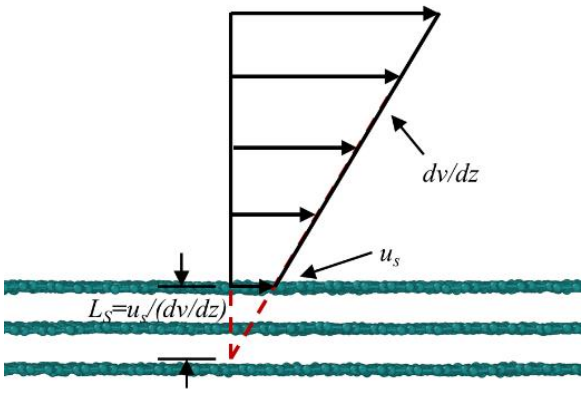

Figure 4. Schematic of the velocity profile in Couette flow and the calculation of the hydrodynamic slip from MD-derived data.

3. Results and Discussion

L_S values were computed for the different interface models using the methodology described in Section 2.3, and the variation of L_S as a function of $\dot{\gamma}_a$ is depicted in Figure 5(a). It can be observed that L_S showcases a bimodal behavior across all interface models, where the symbols in Figure 5(a) can be cross-referenced to Table 1. At low shear rates (LSR) $\dot{\gamma}_a < 3 \times 10^{10}\ \mathrm{s}^{-1}$, L_S in the LSR region, or L_{LSR}, can be averaged to a constant value that depends on the interface model; slip then sharply increases at $\dot{\gamma}_a > 4 \times 10^{10}\ \mathrm{s}^{-1}$, which we called the high shear rate (HSR) regime where L_S saturates (on average) to new constant values (L_{HSR}) greater than those observed in LSR; lastly, a small transition region roughly defined by $3 \times 10^{10}\ \mathrm{s}^{-1} < \dot{\gamma}_a < 4 \times 10^{10}\ \mathrm{s}^{-1}$, acts as a buffer between the two distinct shear rate regimes. A good match between the average L_{LSR} and previous EMD calculations of

L_S[39] was observed, where the deviations of L_{LSR} for O1, O2, O3, H1, and H2 were 0.59%, 3.9%, 26.2%, 6.1%, and 16.4%, respectively. LSR slip matching EMD data has been reported and confirms the consistency of our calculations with previous contributions.[23,24,28]

The sharp increase in L_S with shear rate aligns with prior investigations.[29,30] This can be physically explained from the point of view of the net effect of solid-liquid adhesion and mechanical energy imparted to the fluid. In other words, as the shear rate increases, the fluid molecules near the wall attain sufficient energy to overcome the wall attraction; this is known as the Perierls-Nabarro barrier.[66] Similarly, Martini et al.[29] reported the existence of an inverse relation between the slip jump and wall friction factor. In their work, Martini et al., [29] explained the early reports of the unbounded growth of L_S as the shear rate increases [22–26], where a sharp increase in L_S tends to infinity as the friction factor tends to zero in early nanochannel models where the solid atoms were frozen to save computational power. Alternatively, a finite growth of L_S can be observed in flexible wall models as the wall friction factor is not zero. Furthermore, Li et al.[30] reported in their experimental investigation of Poiseuille flow in silicon nanochannels that when the external force (imparted by a pressure gradient) matched the liquid-wall attraction force, slip jump occurred in a narrow region of shear rate. And upon further increasing the shear rate, L_S measurements became constant.

It is essential to highlight the distinction between $\dot{\gamma}_a$ and $\dot{\gamma}_f$, as they may not be identical.[15,31] $\dot{\gamma}_a$ indicates the magnitude of the externally imposed shear in the system; thus, all interface models were subjected to the same $\dot{\gamma}_a$ to induce shear-driven flow. In contrast, $\dot{\gamma}_f$ represents the shear rate experienced by the fluid, and it is calculated as the slope of the velocity profile for each system. Figure 5(b) illustrates the variation of L_S as a function of $\dot{\gamma}_f$ for the different interface models considered; this is a fundamental relationship needed to further understand the slip response of a system to the shear applied to the fluid. Noticeable differences are readily seen between Figures 5(a) and 5(b): (i) the range of shear rate is reduced by an order of magnitude, such that overall $\dot{\gamma}_f < \dot{\gamma}_a$ and (ii) the transition from L_{LSR} to L_{HSR} does not occur over a narrow shear rate region, but it is now interface-model- and L_S-dependent. The transition regions for O1, O2, O3, H1, and H2 cover the range of 1.6 - 2.31×10^9, 2 - 2.98×10^9, 3.9 - 6×10^9, 3 - 4.54×10^9, and 1.1 - 1.6×10^{10} s^{-1}, respectively, as shown in Figure 5(b). As we will demonstrate, the explanation for the differences between the behavior of L_S as a function of $\dot{\gamma}_f$ or $\dot{\gamma}_a$ is attributed to the interface-model-dependent-availability of momentum carriers.

The main reason why $\dot{\gamma}_f \neq \dot{\gamma}_a$ is that the magnitude of $\dot{\gamma}_f$ is contingent upon the presence of momentum carrier molecules at the solid-liquid interface (i.e., the solid-liquid momentum transfer capability of each interface model), and given that each interface model attracts water molecules at the interface differently, the availability of these momentum carriers will vary across systems. As previously demonstrated by Ramos-Alvarado et al.[38], the availability of momentum carriers is a function of the LJ parameters used to model the non-bonded solid-liquid interactions. The interplay of these parameters will determine the closeness (equilibrium distance) of the liquid particles to the solid

atoms and the concentration (particle count per unit volume) of interfacial liquid molecules. To effectively compare the availability of momentum carriers at the solid-liquid interface among different systems, the density depletion length (δ) serves as a valuable metric,[39,41] where Eq. (2) was used to calculate it from the density profiles depicted in Figure 2. A large positive value of δ indicates a deficit of interfacial momentum carriers, while negative numbers represent a surplus. Table 1 summarizes the δ calculations for all interface models, where no negative values were obtained but only small positive numbers. The interface models O1, O3, and H2 had the largest, intermediate, and smallest δ, respectively. The peak densities of O1, O3, and H2 were 2.67, 2.74, and 3.75 g/cm^3, respectively, as illustrated in Figure 2. Moreover, the density peaks reflect the liquid concentration at the interface. Hence, H2 showed the highest concentration and the shortest equilibrium distance, while O1 displayed the opposite trend, as shown in Figure 2. Consequently, the momentum transfer in model O1 is not highly effective and has the smallest $\dot{\gamma}_f$, while H2 has the highest $\dot{\gamma}_f$ and the most effective momentum transfer, as illustrated in Figure 5(b). The explanation of $\dot{\gamma}_f$ in terms of δ can be extended to better explain the L_S behavior, but first, let us contrast the traditional interpretation of slip based on adhesion metrics.

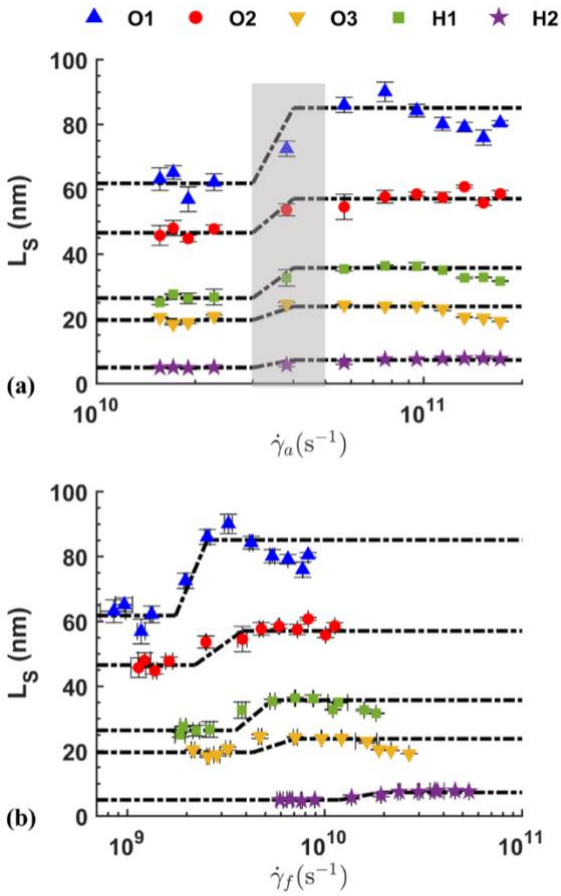

Figure 5. (a) Variation of hydrodynamic slip (L_S) as a function of the applied shear rate ($\dot{\gamma}_a$). The gray-shaded region indicates the transition from L_{LSR} to L_{HSR}. (b) Variation of hydrodynamic slip (L_S) as a

function of the fluid shear rate ($\dot{\gamma}_f$). The black dashed lines are guides for the eye and represent the average value of L_{LSR} and L_{HSR}.

The contact angle (θ) serves as an important solid-liquid affinity metric and thus has been extensively used to characterize interfacial transport properties such as heat transfer[67–69] and hydrodynamic slip.[22,35–37,40,70] In the current work, we have used the θ values calculated elsewhere[39] for the interface models investigated herein; see Table 1. Figure 6(a) depicts L_{LSR} and L_{HSR} as a function of θ for the different interface models, where a few notable observations can be made. First, the solid-liquid affinity for model H2 is so high that θ could not be resolved, and full liquid spreading was observed; see Table 1. This is a limitation in the utilization of θ for the characterization of any transport property in strongly bonded solid-liquid interfaces. Secondly, while the scaling laws[36,40] $L_S \sim (1+\cos\theta)^{-2}$ and $L_S \sim (180-\theta)^{-2}$ seemed to fit a couple of data points (O2 and H1) in the LSR and HSR regimes, the carbon-oxygen-only interface interaction models present a challenge to these theoretical expressions when considered as a group. The interface LJ parameters of O1-O3 were optimized such that they yielded the same θ, binding energy, work of adhesion, and any other solid-liquid affinity property. Nonetheless, they exhibited distinct depletion lengths, different $\dot{\gamma}_f$, and thus a widely ranging L_S from 62.11 to 19.81 nm in the LSR and 83.48 to 23.09 nm in the HSR.

As anticipated from the discussion on the fluid shear rate and its relationship with the solid-liquid momentum transfer ability of each model and motivated by the failure of interfacial affinity metrics to explain slip behavior, L_{LSR} and L_{HSR} are plotted against δ in Figures 6(b) and 6(c) for all interface models. In Figures 6(b) and 6(c), δ is the value calculated in equilibrium conditions (no shear, see Table 1), similar to the early reports by Sendner et al.[40] and Huang et al.[36], who also investigated shear-driven flow. Figure S3 depicts a slight effect on the density profile; thus, we calculated δ for three different shear rates and observed minor deviations (less than 3%) from the equilibrium value, see Table S1. Regarding the data fitting depicted in Figure 6(b), we used the scaling relation $L_S \sim \delta^4$ formulated by Sendner et al.[40] and Huang et al.[36] from scaling a mean field model of wettability and a Green-Kubo-like model of slip. The quality of the data fit using $L_S \sim \delta^4$ produced R^2 values of 0.88 and 0.84 for L_{LSR} and L_{HSR}, respectively. Furthermore, the $L_S \sim \delta^4$ fitting could not capture slip length trends for the most hydrophilic (H2) and hydrophobic (O1) interfaces. Alternatively, Paniagua-Guerra et al.[39] reported that the trends of equilibrium slip lengths across various interface models in graphite-water nanochannel could be effectively captured by an empirical exponential fit ($L_S \sim e^{B\delta}$). Therefore, two exponential functions were employed to fit the shear-driven L_{LSR} and L_{HSR}, where $L_{LSR} = A_{LSR}e^{B_{LSR}\delta}$ and $L_{HSR} = A_{HSR}e^{B_{HSR}\delta}$, see the caption of Figure 6 for the value of the fitting parameters. The R^2 values for the fitted curves were 0.976 and 0.953 for L_{LSR} and L_{HSR}, respectively, indicating a good description of the discrete numerical calculations. Figure 6(c) illustrates how δ adequately captured the slip behavior for the two shear rate regimes and the different interfaces,

including the particularly interesting O1-O3 models, where these shared identical adhesion properties but generated different interfacial liquid properties. These findings highlight the limitations of interfacial affinity metrics in describing L_S in shear-driven flow and suggest that δ is an important parameter to be considered in future surface engineering efforts for designing nanofluidic devices. Since δ is a sub-nanometer scale parameter and thus difficult to measure, MD interface models should be informed by extensive electronic structure calculations that adequately determine the solid-liquid equilibrium distance and binding energy.

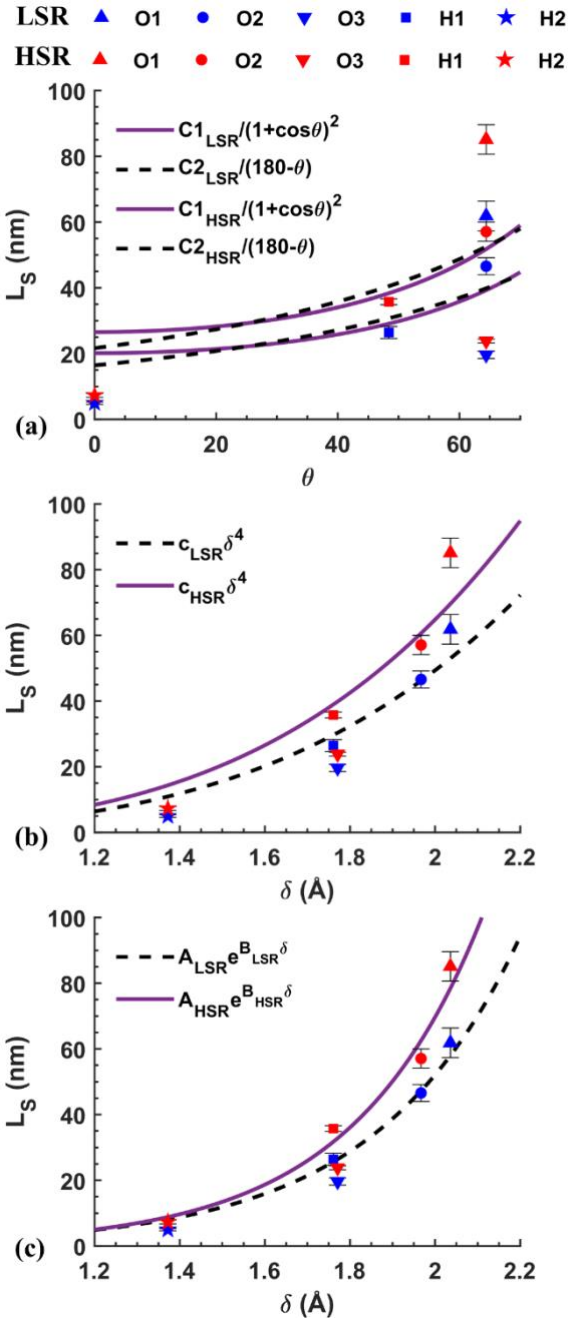

Figure 6. (a) L_{LSR} and L_{HSR} as a function of θ in degree. The black solid and dashed lines are curve fits for L_{LSR} using two different scaling relations, where the fitting parameters are $C1_{LSR}$ = 80.55 nm and $C2_{LSR}$= 5.324×10^5nm. The magenta solid and dashed lines are curve fits for L_{HSR} using two different

scaling relations, where the fitting parameters are $C1_{HSR}$= 106.2 nm and $C2_{HSR}$= 7.015×10^5 nm. (b) L_{LSR} and L_{HSR} as a function of δ. The black dashed line is the fitting curve $L_{LSR} = c_{LSR}\delta^4$, where c_{LSR} = 3.084 nmÅ^{-4}. The black solid line is the fitting curve $L_{HSR} = c_{HSR}\delta^4$, where c_{HSR} =4.05 nmÅ^{-4}. (c) L_{LSR} and L_{HSR} as a function of δ. The black dashed line is the fitting curve $L_{LSR} = A_{LSR}e^{B_{LSR}\delta}$, where A_{LSR}=0.1385 nm and B_{LSR}=3.009 Å^{-1}. The magenta solid line is the fitting curve for $L_{HSR} = A_{HSR}e^{B_{HSR}\delta}$, where A_{HSR}=0.0965 nm and B_{HSR}=3.291Å^{-1}.

Our results quantify the efficacy of momentum transfer from solid to liquid atoms in shear-driven flow using δ for the different interface models. Since we need to apply substantially high shear rates for noise reduction of the MD data, there is momentum transfer from the top solid slab to the liquid and from the liquid to the bottom solid slab. Figure 7 illustrates a modeling artifact observed in high shear conditions, where the bottom slab underwent slight sliding due to momentum transfer from the liquid to the bottom solid slab. Notably, the momentum transfer from the liquid to the bottom solid atoms can be qualitatively assessed by δ. With O1 exhibiting the highest δ (lower momentum carrier availability), the momentum transfer from the liquid to the bottom solid slab is minimal; consequently, the bottom solid slab remains stationary, as depicted in Figure 7. Conversely, H2 experienced the highest momentum transfer due to the small δ value (higher momentum carrier availability); thus, the bottom solid slab had a detectable sliding velocity. Video1 in the Supplemental Material shows the sliding velocity of the bottom graphite slab (H2 model), and sample velocity profiles of the liquid and bottom solid slab for all interface models are presented in Figure S7 for $\dot{\gamma}_a$=$7.6 \times 10^{10}\ s^{-1}$. These observations call for the assessment and mitigation of the bottom slab sliding in similar modeling efforts. This artifact must be either considered in the calculations of slip length [L_S=(u_s-u_{mw})/($\partial u/\ \partial z$)], where u_s, u_{mw} represent water slip velocity and the velocity of the innermost graphite layer of the sliding bottom slab, respectively) or eliminated from the NEMD models by restricting the momentum in the applied shear direction of the theoretically stationary solid slab (see Figure S8 for the velocity profile with the stationary bottom slab). In our calculation, the sliding velocity was eliminated by restricting the momentum in the applied shear direction.

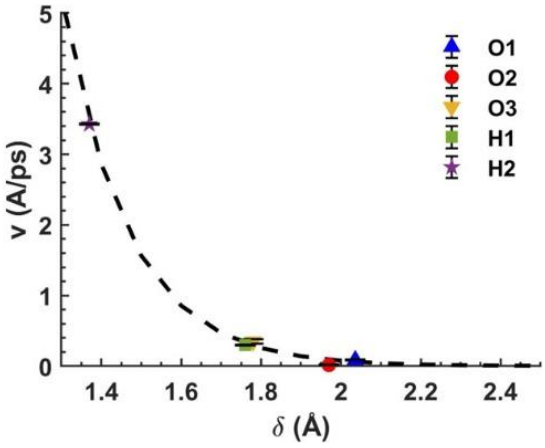

Figure 7. Variation of the bottom graphite slab velocity with respect to the depletion length (δ) at a shear rate of $\dot{\gamma}_a$=7.6 × 10^{10} s^{-1}. The black dashed line is a guide to the eye.

To comprehend the LSR-to-HSR hydrodynamic slip transition, and to add to previous findings, we investigated the rheological properties of water under the effects of shear. Recent research has indicated that water confined in nanoscale graphite slits exhibits shear-thinning behavior at high shear rates[71]. Similarly, NEMD studies of Couette flow demonstrated a transition from Newtonian fluid behavior at low shear rates to non-Newtonian behavior at high shear rates[72,73]. In the current investigation, the shear viscosity of nanoconfined water was computed following[71]:

$$\tau_{xy} = \frac{F_{x,top}}{A_{xy}} \tag{3}$$

$$\mu = \frac{\tau_{xy}}{\dot{\gamma}_f} \tag{4}$$

where τ_{xy} is the shear stress, A_{xy} is the cross-section area of the graphite slab, $F_{x,top}$ is the viscous shear force derived from NEMD simulations, and μ is the shear viscosity. The shear force was computed by adding all forces exclusively generated by the water-carbon interactions on the top graphene slab in the direction of flow. Additionally, we calculated the friction coefficient:

$$\eta = \frac{\tau_{xy}}{u_s} \tag{5}$$

where the combined response of μ and η to shear (and thus temperature) will allow for a better explanation of the bimodal L_s response, given that L_S=μ/η.

The variation of μ with the applied shear rate is illustrated in Figure 8(a). It is evident that water exhibited a different rheological response from LSR to HSR, as illustrated in the bimodal rate of change from LSR to HSR. For more detailed information, Figure S9 illustrates the τ_{xy} vs $\dot{\gamma}_f$ relationship for all individual interface models. It is noted that μ in LSR had an average value of 0.632 ± 0.0273 mPa-s, as shown in Figure 8(a). In a previous contribution, Hess[74] performed periodic perturbation simulation with the SPC/E water model to find $\mu = 0.642 \pm 0.008$ mPa-s, which matches our estimation of μ in the LSR regime. Conversely, μ noticeably decreased in the HSR regime

exhibiting shear-thinning behavior, see Figure 8(a). Like μ, η decreased as a function of shear in a bimodal fashion where either a nearly constant or small rate of reduction was observed, as shown in Figure 8(b). This finding aligned with the previous studies where the friction coefficient was observed constant at shear rates of approximately ~10^9 s^{-1}.[25,75,76] Nonetheless, past the transition region, η decreased at a higher rate in the HSR. This phenomenon is consistent with previous findings by Wagemann et al.[25], who reported a similar response of η for graphite and water. Ultimately, the similar shear rate response of μ and η in the LSR, and the dominant reduction rate of η led to the observed sudden slip jump from the LSR to HSR regime depicted in Figure 5. Our claims are supported by calculations of L_S=μ/η and reported in Figure S10.

While Figure 8 (a)-(b) allow visualizing the range of variation of the magnitudes of μ and η as a function of the applied shear rate, and quantitatively explains the shear rate response of L_S in Figure S10, unifying these parameters on the same graph facilitates a better explanation of the bimodal response of L_S. Figure 8(c) depicts the normalized μ and η for model H2. It can be observed that when normalized and unified, μ and η vary at the same rate in the LSR; thus, resulting in the observed L_{LSR} magnitude. Alternatively, in the LSR-to-HSR transition, η decreases at a faster rate than μ, and finally in the HSR μ and η run in parallel, which explains the L_{LSR}-to-L_{HSR} jump, transition, and bimodal response of L_S to shear rate.

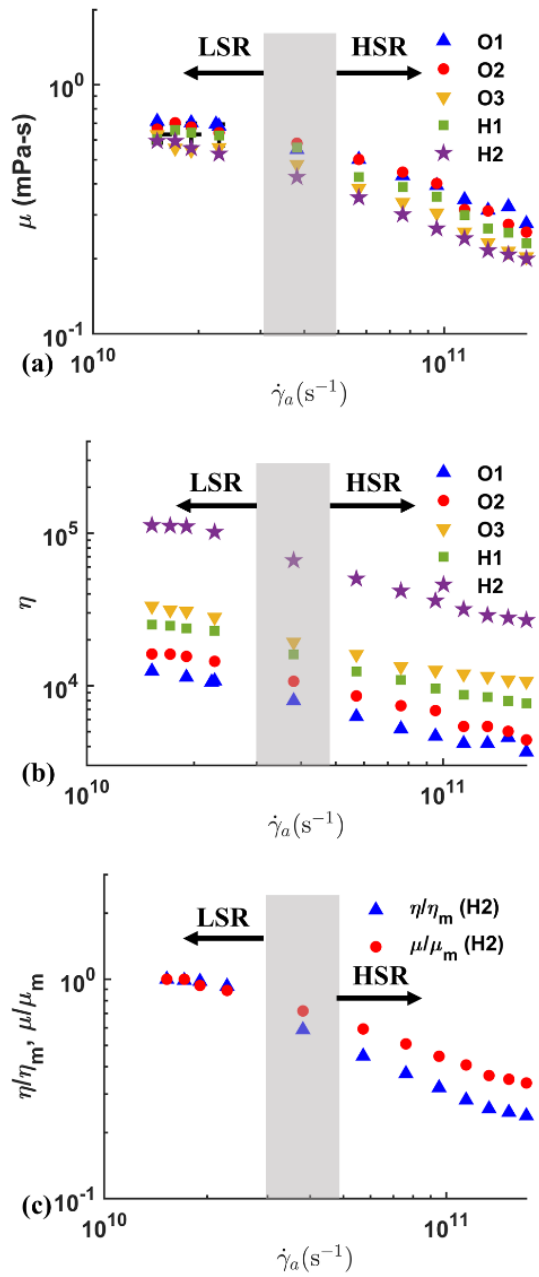

Figure 8. (a) Variation of the averaged μ with respect to $\dot{\gamma}_a$. (b) Variation of the averaged η with respect to $\dot{\gamma}_a$. (c) Variation of the normalized averaged μ and η with respect to $\dot{\gamma}_a$ for the H2 interface model. The gray-shaded region indicates the transition from the LSR to HRS regime.

As indicated in Figure 5, L_{LSR} increased to L_{HSR} for all interface models and this so-called slip jump was a function of the shear rate and δ. When quantified, L_{HSR} was 1.28 times higher on average than L_{LSR} across all interface models, as depicted in Figure 9. Furthermore, L_S was also computed for the TIP4P/2005 water model to investigate the observed slip jump further. Figure S11 of the Supplementary Material depicts all interfacial density profiles and L_S data for the TIP4P/2005 water model calculations. It is noteworthy that the slip jump for both the SPC/E and TIP4P/2005 water

models showed good consistency. The estimated slip jump $\frac{L_{HSR}}{L_{LSR}} = 1.28$ for all interface models resulted in an average and maximum error of ~6% and ~15%, respectively. While significant, this finding calls for further computational verification and theoretical analysis of this seemingly constant slip jump, which apparently is independent of the interface model parameters and water model but could be exclusive for graphite-water systems or interfaces of similar smoothness. This relationship could likely be broken down for solid interfaces that are naturally rougher, such as crystalline diamond 100 surfaces or amorphous interfaces.

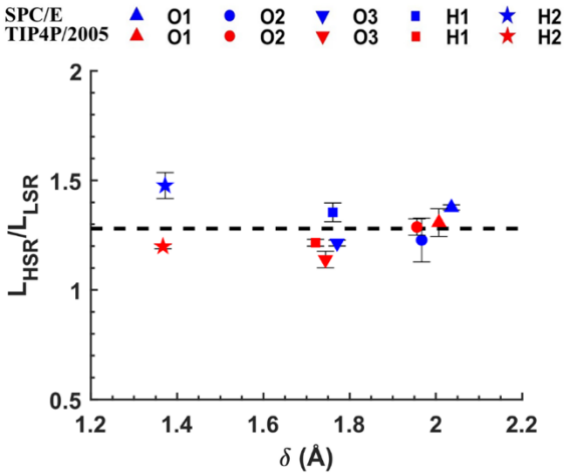

Figure 9. Slip jump ratio $\frac{L_{HSR}}{L_{LSR}}$ for all interface models. On average, the slip jump was 1.28 for both the SPC/E (blue markers) and TIP4P/2005 (red markers) water models.

Table 2. Slip jump ($\frac{L_{HSR}}{L_{LSR}}$) for SPC/E and TIP4P/2005 water models

Model	$\frac{L_{HSR}}{L_{LSR}}$ (SPC/E)	$\frac{L_{HSR}}{L_{LSR}}$ (TIP4P/2005)
O1	1.38±0.01	1.31±0.06
O2	1.23±0.10	1.29±0.04
O3	1.21±0.01	1.14±0.04
H1	1.35±0.04	1.22±0.02
H2	1.48±0.06	1.20±0.01

4. Conclusions

In this investigation, hydrodynamic slip was numerically investigated for five distinct graphite-water interface models (i.e., different non-bonded solid-liquid interaction parameters) via NEMD

simulations of shear-driven flow. Graphite-water interfaces were selected for this investigation due to being dominated by non-bonded interactions and for being amply characterized in the literature. Our findings showed that the density depletion length δ, which quantifies the availability of interfacial momentum carriers, could (1) adequately describe the trends in slip length of both the low shear rate regime (LSR) and the high shear rate regime (HSR) for the different interface models, (2) the different response of the interface models to the shear rate experienced by the fluid, and (3) the amount of sliding of the theoretically fixed solid slab in NEMD models of shear driven flow. It was found that L_S in the LSR showed a good agreement with previous equilibrium molecular dynamics (EMD) data. As $\dot{\gamma}_a$ increased, L_S exhibited a distinctive behavior — L_S sharply increased and eventually asymptote to a constant value in the HSR. The combined effect of viscosity and the friction coefficient contributed to explaining this observation: the water viscosity and friction coefficient either remained constant for very low shear or decreased at a similar rate in the LSR; alternatively, shear-thinning behavior and a faster-decreasing rate in the friction coefficient were observed in the HSR, thus contributing to a sudden increase in L_S. Moreover, our study unveiled a consistent finding across all interfaces and two different water models, where L_S values in the HSR were, on average, 1.28 times greater than those in the LSR, with an average deviation of ~6% from this hypothetical constant factor.[33]

Supplemental Materials

The data that support the findings of this study are available within its supplementary material.

Acknowledgments

This research is supported by the National Science Foundation, USA (Award number: 2241730).

AUTHOR DECLARATIONS

Conflict of Interest

The authors have no conflicts to disclose.

References

[1] B. Radha, A. Esfandiar, F.C. Wang, A.P. Rooney, K. Gopinadhan, A. Keerthi, A. Mishchenko, A. Janardanan, P. Blake, L. Fumagalli, M. Lozada-Hidalgo, S. Garaj, S.J. Haigh, I. V. Grigorieva, H.A. Wu, and A.K. Geim, "Molecular transport through capillaries made with atomic-scale precision," Nature **538**(7624), 222–225 (2016).

[2] D. Mijatovic, J.C.T. Eijkel, and A. Van Den Berg, "Technologies for nanofluidic systems: Top-down vs. bottom-up - A review," Lab Chip **5**(5), 492–500 (2005).

[3] D. Cohen-Tanugi, and J.C. Grossman, "Water desalination across nanoporous graphene," Nano Lett **12**(7), 3602–3608 (2012).

[4] S. Homaeigohar, and M. Elbahri, "Graphene membranes for water desalination," NPG Asia Mater **9**(8), e427–e427 (2017).

[5] S. Rikhtehgaran, and A. Lohrasebi, "Water desalination by a designed nanofilter of graphene-charged carbon nanotube: A molecular dynamics study," Desalination **365**, 176–181 (2015).

[6] H. Daiguji, P. Yang, A.J. Szeri, and A. Majumdar, "Electrochemomechanical energy conversion in nanofluidic channels," Nano Lett **4**(12), 2315–2321 (2004).

[7] A. Siria, P. Poncharal, A.L. Biance, R. Fulcrand, X. Blase, S.T. Purcell, and L. Bocquet, "Giant osmotic energy conversion measured in a single transmembrane boron nitride nanotube," Nature **494**(7438), 455–458 (2013).

[8] R. Karnik, C. Duan, K. Castelino, H. Daiguji, and A. Majumdar, "Rectification of ionic current in a nanofluidic diode," Nano Lett **7**(3), 547–551 (2007).

[9] Y. Liu, L. Guo, X. Zhu, Q. Ran, and R. Dutton, "Suppression of ion conductance by electro-osmotic flow in nano-channels with weakly overlapping electrical double layers," AIP Adv **6**(8), 085022 (2016).

[10] W. Sun, P. Qin, H. Gao, G. Li, and K. Jiao, "Electrochemical DNA biosensor based on chitosan/nano-V2O5/MWCNTs composite film modified carbon ionic liquid electrode and its application to the LAMP product of Yersinia enterocolitica gene sequence," Biosens Bioelectron **25**(6), 1264–1270 (2010).

[11] Z. Mazibuko, Y.E. Choonara, P. Kumar, L.C. Du Toit, G. Modi, D. Naidoo, and V. Pillay, "A Review of the Potential Role of Nano-Enabled Drug Delivery Technologies in Amyotrophic Lateral Sclerosis: Lessons Learned from Other Neurodegenerative Disorders," J Pharm Sci **104**(4), 1213–1229 (2015).

[12] L. Bocquet, and E. Charlaix, "Nanofluidics, from bulk to interfaces," Chem Soc Rev **39**(3), 1073–1095 (2010).

[13] J.A. Thomas, and A.J.H. McGaughey, "Water Flow in Carbon Nanotubes: Transition to Subcontinuum Transport," Phys Rev Lett **102**(18), 184502 (2009).

[14] D.C. Tretheway, and C.D. Meinhart, "Apparent fluid slip at hydrophobic microchannel walls," Physics of Fluids **14**(3), L9–L12 (2002).

[15] X. Yong, and L.T. Zhang, "Slip in nanoscale shear flow: Mechanisms of interfacial friction," Microfluid Nanofluidics **14**(1–2), 299–308 (2013).

[16] P.M. Navier, "Memoire sur les lois du mouvement des fluides," Mem.Acad.Sci. **6**, 389–440 (1823).

[17] M. Majumder, N. Chopra, R. Andrews, and B.J. Hinds, "Nanoscale hydrodynamics: Enhanced flow in carbon nanotubes," Nature **438**(7064), 44–44 (2005).

[18] J.K. Holt, H.G. Park, Y. Wang, M. Stadermann, A.B. Artyukhin, C.P. Grigoropoulos, A. Noy, and O. Bakajin, "Fast Mass Transport Through Sub-2-Nanometer Carbon Nanotubes," Science (1979) **312**(5776), 1034–1037 (2006).

[19] L. Hilaire, B. Siboulet, S. Charton, and J.F. Dufrêche, "Liquid-Liquid Flow at Nanoscale: Slip and Hydrodynamic Boundary Conditions," Langmuir **39**(6), 2260–2273 (2023).

[20] J.H. Choo, R.P. Glovnea, A.K. Forrest, and H.A. Spikes, "A low friction bearing based on liquid slip at the wall," J Tribol **129**(3), 611–620 (2007).

[21] J.H. Choo, H.A. Spikes, M. Ratoi, R. Glovnea, and A. Forrest, "Friction reduction in low-load hydrodynamic lubrication with a hydrophobic surface," Tribol Int **40**(2 SPEC. ISS.), 154–159 (2007).

[22] R.S. Voronov, D. V. Papavassiliou, and L.L. Lee, "Boundary slip and wetting properties of interfaces: Correlation of the contact angle with the slip length," Journal of Chemical Physics **124**(20), 204701 (2006).

[23] S.K. Kannam, B.D. Todd, J.S. Hansen, and P.J. Daivis, "Slip flow in graphene nanochannels," Journal of Chemical Physics **135**(14), 144701 (2011).

[24] S. Kumar Kannam, B.D. Todd, J.S. Hansen, and P.J. Daivis, "Slip length of water on graphene: Limitations of non-equilibrium molecular dynamics simulations," Journal of Chemical Physics **136**(2), 024705 (2012).

[25] E. Wagemann, E. Oyarzua, J.H. Walther, and H.A. Zambrano, "Slip divergence of water flow in graphene nanochannels: The role of chirality," Physical Chemistry Chemical Physics **19**(13), 8646–8652 (2017).

[26] P.A. Thompson, and S.M. Troian, "A general boundary condition for liquid flow at solid surfaces," Nature **389**(6649), 360–362 (1997).

[27] A. Alizadeh Pahlavan, and J.B. Freund, "Effect of solid properties on slip at a fluid-solid interface," Phys Rev E Stat Nonlin Soft Matter Phys **83**(2), 021602 (2011).

[28] B. Ramos-Alvarado, S. Kumar, and G.P. Peterson, "Hydrodynamic slip length as a surface property," Phys Rev E **93**(2), 023101 (2016).

[29] A. Martini, H.-Y. Hsu, N.A. Patankar, and S. Lichter, "Slip at High Shear Rates," Phys Rev Lett **100**(20), 206001 (2008).

[30] L. Li, J. Mo, and Z. Li, "Flow and slip transition in nanochannels," Phys Rev E Stat Nonlin Soft Matter Phys **90**(3), 033003 (2014).

[31] X. Yong, and L.T. Zhang, "Thermostats and thermostat strategies for molecular dynamics simulations of nanofluidics," J Chem Phys **138**(8), 084503 (2013).

[32] H. Oga, T. Omori, L. Joly, and Y. Yamaguchi, "Equilibrium molecular dynamics evaluation of the solid-liquid friction coefficient: role of timescales," J Chem Phys **159**(2), 024701 (2023).

[33] L. Maffioli, J.P. Ewen, E.R. Smith, S. Varghese, P.J. Daivis, D. Dini, and B.D. Todd, "TTCF4LAMMPS: A toolkit for simulation of the non-equilibrium behaviour of molecular fluids at experimentally accessible shear rates," Comput Phys Commun **300**, 109205 (2024).

[34] L. Maffioli, E.R. Smith, J.P. Ewen, P.J. Daivis, D. Dini, and B.D. Todd, "Slip and stress from low shear rate nonequilibrium molecular dynamics: The transient-time correlation function technique," J Chem Phys **156**(18), 184111 (2022).

[35] R.S. Voronov, D. V. Papavassiliou, and L.L. Lee, "Slip length and contact angle over hydrophobic surfaces," Chem Phys Lett **441**(4–6), 273–276 (2007).

[36] D.M. Huang, C. Sendner, D. Horinek, R.R. Netz, and L. Bocquet, "Water Slippage versus Contact Angle: A Quasiuniversal Relationship," Phys Rev Lett **101**(22), 226101 (2008).

[37] T.A. Ho, D. V. Papavassiliou, L.L. Lee, and A. Striolo, "Liquid water can slip on a hydrophilic surface," Proceedings of the National Academy of Sciences **108**(39), 16170–16175 (2011).

[38] B. Ramos-Alvarado, S. Kumar, and G.P. Peterson, "Wettability transparency and the quasiuniversal relationship between hydrodynamic slip and contact angle," Appl Phys Lett **108**(7), 074105 (2016).

[39] L.E. Paniagua-Guerra, C.U. Gonzalez-Valle, and B. Ramos-Alvarado, "Effects of the Interfacial Modeling Approach on Equilibrium Calculations of Slip Length for Nanoconfined Water in Carbon Slits," Langmuir **36**(48), 14772–14781 (2020).

[40] C. Sendner, D. Horinek, L. Bocquet, and R.R. Netz, "Interfacial water at hydrophobic and hydrophilic surfaces: Slip, viscosity, and diffusion," Langmuir **25**(18), 10768–10781 (2009).

[41] L.E. Paniagua-Guerra, and B. Ramos-Alvarado, "Thermal transport across flat and curved gold-water interfaces: Assessing the effects of the interfacial modeling parameters," Journal of Chemical Physics **158**(13), 134717 (2023).

[42] S. Plimpton, "Fast Parallel Algorithms for Short-Range Molecular Dynamics," J Comput Phys **117**(1), 1–19 (1995).

[43] A. Stukowski, "Visualization and analysis of atomistic simulation data with OVITO-the Open Visualization Tool," Model Simul Mat Sci Eng **18**(1), 015012 (2010).

[44] F. Taherian, V. Marcon, N.F.A. Van Der Vegt, and F. Leroy, "What is the contact angle of water on graphene?," Langmuir **29**(5), 1457–1465 (2013).

[45] B. Ramos-Alvarado, "Water wettability of graphene and graphite, optimization of solid-liquid interaction force fields, and insights from mean-field modeling," Journal of Chemical Physics **151**(11), 114701 (2019).

[46] S. Nosé, "A molecular dynamics method for simulations in the canonical ensemble," Mol Phys **52**(2), 255–268 (1984).

[47] W.G. Hoover, "Canonical dynamics: Equilibrium phase-space distributions," Phys Rev A (Coll Park) **31**(3), 1695–1697 (1985).

[48] J.-P. Ryckaert, G. Ciccotti, and H.J.C. Berendsen, "Numerical integration of the cartesian equations of motion of a system with constraints: molecular dynamics of n-alkanes," J Comput Phys **23**(3), 327–341 (1977).

[49] G. Ciccotti, and J.P. Ryckaert, "Molecular dynamics simulation of rigid molecules," Computer Physics Reports **4**, 346–392 (1986).

[50] R.W. Hockney, and J.W. Eastwood, *Computer Simulation Using Particles* (CRC Press, 1988).

[51] L. Lindsay, and D.A. Broido, "Optimized Tersoff and Brenner empirical potential parameters for lattice dynamics and phonon thermal transport in carbon nanotubes and graphene," Phys Rev B Condens Matter Mater Phys **81**(20), 205441 (2010).

[52] L. Lindsay, D.A. Broido, and N. Mingo, "Flexural phonons and thermal transport in multilayer graphene and graphite," Phys Rev B Condens Matter Mater Phys **83**(23), 235428 (2011).

[53] B. Ramos-Alvarado, S. Kumar, and G.P. Peterson, "Wettability of graphitic-carbon and silicon surfaces: MD modeling and theoretical analysis," Journal of Chemical Physics **143**(4), 044703 (2015).

[54] J. Ma, A. Michaelides, D. Alfè, L. Schimka, G. Kresse, and E. Wang, "Adsorption and diffusion of water on graphene from first principles," Phys Rev B Condens Matter Mater Phys **84**(3), 033402 (2011).

[55] Y. Wu, and N.R. Aluru, "Graphitic carbon-water nonbonded interaction parameters," Journal of Physical Chemistry B **117**(29), 8802–8813 (2013).

[56] E. Voloshina, D. Usvyat, M. Schütz, Y. Dedkov, and B. Paulus, "On the physisorption of water on graphene: a CCSD(T) study," Physical Chemistry Chemical Physics **13**(25), 12041–12047 (2011).

[57] R. Khare, P. Keblinski, and A. Yethiraj, "Molecular dynamics simulations of heat and momentum transfer at a solid–fluid interface: Relationship between thermal and velocity slip," Int J Heat Mass Transf **49**(19–20), 3401–3407 (2006).

[58] P.A. Thompson, and M.O. Robbins, "Shear flow near solids: Epitaxial order and flow boundary conditions," Phys Rev A (Coll Park) **41**(12), 6830–6837 (1990).

[59] Z. Zhang, H. Zhang, and H. Ye, "Pressure-driven flow in parallel-plate nanochannels," Appl Phys Lett **95**(15), 154101 (2009).

[60] J.A. Thomas, and A.J.H. McGaughey, "Reassessing fast water transport through carbon nanotubes," Nano Lett **8**(9), 2788–2793 (2008).

[61] S. Bernardi, B.D. Todd, and D.J. Searles, "Thermostating highly confined fluids," J Chem Phys **132**(24), 244706 (2010).

[62] R. Khare, J. De Pablo, and A. Yethiraj, "Molecular simulation and continuum mechanics study of simple fluids in non-isothermal planar couette flows," Journal of Chemical Physics **107**(7), 2589–2596 (1997).

[63] S.Y. Liem, D. Brown, and J.H.R. Clarke, "Investigation of the homogeneous-shear nonequilibrium-molecular-dynamics method," Phys Rev A (Coll Park) **45**(6), 3706–3713 (1992).

[64] J.S. Hansen, B.D. Todd, and P.J. Daivis, "Prediction of fluid velocity slip at solid surfaces," Phys Rev E **84**(1), 016313 (2011).

[65] G. Nagayama, and P. Cheng, "Effects of interface wettability on microscale flow by molecular dynamics simulation," Int J Heat Mass Transf **47**(3), 501–513 (2004).

[66] O.M. Braun, and Y.S. Kivshar, "Nonlinear dynamics of the Frenkel–Kontorova model," Phys Rep **306**(1–2), 1–108 (1998).

[67] C.U. Gonzalez-Valle, and B. Ramos-Alvarado, "Molecular Dynamics Simulations of Wettability, Thermal Transport, and Interfacial Liquid Structuring at the Nanoscale in Polar Solid-Liquid Interfaces," ACS Appl Nano Mater **4**(4), 3821–3832 (2021).

[68] B. Ramos-Alvarado, S. Kumar, and G.P. Peterson, "Solid-Liquid Thermal Transport and Its Relationship with Wettability and the Interfacial Liquid Structure," Journal of Physical Chemistry Letters **7**(17), 3497–3501 (2016).

[69] C.U. Gonzalez-Valle, S. Kumar, and B. Ramos-Alvarado, "Thermal Transport across SiC-Water Interfaces," ACS Appl Mater Interfaces **10**(34), 29179–29186 (2018).

[70] R.L. Zhang, Q.F. Di, X.L. Wang, W.P. Ding, and W. Gong, "Numerical study of the relationship between apparent slip length and contact angle by Lattice Boltzmann Method," Journal of Hydrodynamics **24**(4), 535–540 (2012).

[71] F. Li, I.A. Korotkin, and S.A. Karabasov, "Rheology of Water Flows Confined between Multilayer Graphene Walls," Langmuir **36**(20), 5633–5646 (2020).

[72] S. Liu, and X. Yu, "Molecular dynamics study on the slippage of liquid lithium flow in tungsten nanochannels," Nuclear Fusion **63**(3), 036007 (2023).

[73] X. Yong, and L.T. Zhang, "Investigating liquid-solid interfacial phenomena in a Couette flow at nanoscale," Phys Rev E **82**(5), 056313 (2010).

[74] B. Hess, "Determining the shear viscosity of model liquids from molecular dynamics simulations," Journal of Chemical Physics **116**(1), 209–217 (2002).

[75] S. Nakaoka, Y. Yamaguchi, T. Omori, M. Kagawa, T. Nakajima, and H. Fujimura, "Molecular dynamics analysis of the velocity slip of a water and methanol liquid mixture," Phys Rev E **92**(2), 022402 (2015).

[76] S. Nakaoka, Y. Yamaguchi, T. Omori, and L. Joly, "Molecular dynamics analysis of the friction between a water-methanol liquid mixture and a non-polar solid crystal surface.," J Chem Phys **146**(17), 174702 (2017).